Monthly Notices
of the
ROYAL ASTRONOMICAL SOCIETY

MNRAS **498,** 4119–4133 (2020)
Advance Access publication 2020 September 2

doi:10.1093/mnras/staa2065

The tidal disruption event AT 2018hyz – I. Double-peaked emission lines and a flat Balmer decrement

P. Short [1★] M. Nicholl,[1,2] A. Lawrence [1★] S. Gomez,[3] I. Arcavi,[4,5] T. Wevers [6] G. Leloudas,[7] S. Schulze [8] J. P. Anderson,[9] E. Berger,[3] P. K. Blanchard,[10] J. Burke,[11,12] N. Castro Segura,[13] P. Charalampopoulos,[7] R. Chornock,[14] L. Galbany [15] M. Gromadzki,[16] L. J. Herzog,[14] D. Hiramatsu,[11,12] Keith Horne,[17] G. Hosseinzadeh,[3] D. Andrew Howell,[11,12] N. Ihanec,[15] C. Inserra [18] E. Kankare,[19] K. Maguire,[20] C. McCully,[12] T. E. Müller Bravo [13] F. Onori [21] J. Sollerman[22] and D. R. Young[23]

Affiliations are listed at the end of the paper

Accepted 2020 July 10. Received 2020 July 10; in original form 2020 March 11

ABSTRACT

We present results from spectroscopic observations of AT 2018hyz, a transient discovered by the All-Sky Automated Survey for Supernova survey at an absolute magnitude of $M_V \sim -20.2$ mag, in the nucleus of a quiescent galaxy with strong Balmer absorption lines. AT 2018hyz shows a blue spectral continuum and broad emission lines, consistent with previous TDE candidates. High cadence follow-up spectra show broad Balmer lines and He I in early spectra, with He II making an appearance after ∼70–100 d. The Balmer lines evolve from a smooth broad profile, through a boxy, asymmetric double-peaked phase consistent with accretion disc emission, and back to smooth at late times. The Balmer lines are unlike typical active galactic nucleus in that they show a flat Balmer decrement (Hα/H$\beta \sim 1.5$), suggesting the lines are collisionally excited rather than being produced via photoionization. The flat Balmer decrement together with the complex profiles suggests that the emission lines originate in a disc chromosphere, analogous to those seen in cataclysmic variables. The low optical depth of material due to a possible partial disruption may be what allows us to observe these double-peaked, collisionally excited lines. The late appearance of He II may be due to an expanding photosphere or outflow, or late-time shocks in debris collisions.

Key words: black hole physics – galaxies: active – galaxies: individual: AT 2018hyz – transients: tidal disruption events.

1 INTRODUCTION

A tidal disruption event (TDE) is predicted to occur when a star passes within the tidal radius of a supermassive black hole (SMBH). In this region, the tidal force of the black hole is sufficient to overcome the star's self-gravity and tear it apart (Hills 1975). A significant fraction of the resulting stellar debris will be accreted on to the SMBH producing a luminous flare. This can be utilized to probe the properties of SMBHs in both active and quiescent galaxies, particularly at modest BH masses, and could be crucial in our understanding of accretion physics, allowing us to observe the formation of accretion discs, the broad-line region (BLR), and jets.

High-cadence optical surveys have revealed a plethora of nuclear candidates, some with X-ray counterparts and some without (Auchettl, Guillochon & Ramirez-Ruiz 2017). The resulting well-sampled light curves and spectroscopic follow-up, while sharing some similarities, have shown a wide range of luminosities, light curve shapes and spectral features. The peak luminosities of these transients fall in the range of $L_{\rm bol} \sim 10^{41}$–10^{44} erg s^{-1} and are consistent with blackbody temperatures of $T \sim 20\,000$–$50\,000$ K. Their emission fades away over periods of months to years. It is hard to prove that the observed outbursts result from a star being disrupted rather than due to an unusual kind of supernova or an instability in a quiescent active galactic nucleus (AGN) disc, but the circumstantial evidence seems strong. Determining the true nature of these flares requires combining detailed observations with theory and simulations.

The light curves of TDEs were originally predicted to follow a $t^{-5/3}$ power law, matching the fall-back rate of material on to the black hole (Rees 1988; Phinney 1989). While early discoveries of TDE candidates in X-rays agreed well with this prediction (Komossa 2017), more recent optical discoveries have revealed a great diversity in light curve shapes. This suggests that the mechanism behind the flare is not fully understood. It is widely accepted that one of two scenarios dominate the UV + optical emission. One is an accretion disc, which forms from the bound debris. In this scenario, a disc forms as material circularizes and a hot blue continuum is emitted peaking in the UV/X-ray. However, observed temperatures are too low to originate from a compact accretion disc, a problem also seen in AGN (Lawrence 2012). To explain this and the appearance of broad emission lines, some of the emission would have to be reprocessed. Strubbe & Quataert (2009) suggested unbound material could be responsible for the reprocessing. However, Guillochon, Manukian & Ramirez-Ruiz (2014) showed that self-gravity would make the stream of unbound debris thin and thus not likely to reprocess much emission, though material that was initially bound but later unbound due to winds might still be responsible for some

★ E-mail: pshort@roe.ac.uk (PS); al@roe.ac.uk (AL)

or all of the reprocessing. Another source of reprocessing could be a photosphere surrounding the disc (see also Roth et al. 2016). In addition to the temperature problem, time-integrated energies are more than an order of magnitude lower than expected (Piran et al. 2015), which could be explained by a significant amount of emission at unobservable EUV wavelengths, by severe mass-loss during circularization (Metzger & Stone 2016) or by a long tail in the light curve (van Velzen et al. 2019b). Another issue with the accretion disc scenario is that, with some notable exceptions (e.g. Holoien et al. 2016), observations of TDEs have shown the temperature to remain roughly constant as the luminosity declines, when one would expect the temperature to evolve as the disc size or accretion rate changes.

An alternative process is emission produced by shocks in collisions between stellar debris streams (Piran et al. 2015; Shiokawa et al. 2015; Jiang, Guillochon & Loeb 2016; Bonnerot, Rossi & Lodato 2017), though this struggles to produce both X-ray and optical emission simultaneously and also suffers from the missing energy problem. The latter is usually explained by a low radiative efficiency, which Svirski, Piran & Krolik (2017) explain could be the result of an elliptical accretion disc. Light-curve plateaus and late-time X-ray emission have been observed in some TDEs (e.g. Gezari, Cenko & Arcavi 2017; Wevers et al. 2019b). These may be due to delayed accretion disc formation resulting from the stream–stream collisions. If so, one might expect a scenario in which shocks in stream–stream collisions dominate the emission initially, then at later times reprocessed emission from the accretion disc takes over. Dai et al. (2018) suggest a model analogous to the unified model of AGN. Here, the successful detection of X-ray emission depends on viewing angle as emission in the accretion disc plane gets obscured. The viewing angle may also influence the features seen in the optical spectra (Nicholl et al. 2019).

The emission lines featuring in optical TDE spectra show broad ($1-2 \times 10^4$ km s^{-1}; Arcavi et al. 2014), complex, often asymmetric profiles. The spectra of the first optical/ultraviolet TDE featured only He II λ4686 (Gezari et al. 2012) but the ever-increasing sample of events have also shown H I Balmer and He I lines, revealing a continuum of H-rich to He-rich TDEs (Arcavi et al. 2014). In some cases, emission lines have been observed to appear and disappear as the TDE evolves (Hung et al. 2019; Nicholl et al. 2019). In addition, metal lines such as Fe II, O III, and N III have been detected in a number of TDEs. Fe II can be associated with the formation of a compact accretion disc (Wevers et al. 2019b), while O III and N III are attributed to Bowen fluorescence, a mechanism whereby an EUV photon is emitted by recombining He II, which resonates with an O III transition, which, in turn, resonates with a transition in N III (Blagorodnova et al. 2019; Leloudas et al. 2019; Onori et al. 2019). The detection of Bowen lines in X-ray quiet TDEs supports the existence of an obscured EUV/X-ray emission source. van Velzen et al. (2020) find that TDEs showing Bowen lines have smaller radii and a longer rise time in their light curves, putting them in a separate class to other TDEs.

The rich phenomenology of objects classified as TDEs is both fascinating and confusing, and the problems noted – cool temperature and low total energy – are a challenge to theoretical understanding. In this paper, we present densely sampled spectroscopic observations of the TDE candidate AT 2018hyz (ASASSN-18zj), discovered by the All-Sky Automated Survey for Supernova (ASAS-SN; Shappee et al. 2014; Kochanek et al. 2017) and appearing also in the sample of TDEs detected by the Zwicky Transient Facility (ZTF; van Velzen et al. 2020). In Section 2, we present the host galaxy spectrum and follow-up observations, in Section 3, we determine the host black hole mass and analyse emission lines from the transient, in Section 4, we discuss the results and offer our interpretation and in Section 5 we summarize our findings and come to a conclusion. A companion paper, Gomez et al. (2020), discusses photometry, key results from which we use in this paper 1. Gomez et al. (2020) find the peak of the bolometric light curve to be at MJD = 58429 so for consistency we define the epoch of each spectrum relative to this.[1]

2 OBSERVATIONS AND DATA REDUCTION

AT 2018hyz was discovered by ASAS-SN on 2018-11-06.65 (all times in UT) with an apparent g-band magnitude of 16.4 mag (Brimacombe & Stanek 2018), though the earliest ASAS-SN detection of this event was on 2018-10-14.48. The transient was detected at α = 10:06:50.872, δ = + 01:41:34.10, placing it 0.2 ± 0.8 arcsec (Gomez et al. 2020) from the centre of *SDSS J100650.86+014134.0*, an apparently quiescent or post-starburst galaxy at a redshift of z = 0.045 73. Assuming a flat ΛCDM cosmology with H_0 = 69.3 km s^{-1} Mpc^{-1}, Ω_m = 0.286, and Ω_Λ = 0.712 (Hinshaw et al. 2013), the redshift of the host galaxy suggests an absolute g-band magnitude of −20.2 mag. AT 2018hyz was classified as a TDE candidate following spectroscopic observations (Dong et al. 2018), which show a strong blue continuum with broad Balmer lines and He I, similar to other TDE candidates (e.g. Arcavi et al. 2014; Holoien et al. 2014, 2019). The combination of these spectral features, high luminosity and proximity to the nucleus of the host make AT 2018hyz a strong TDE candidate.

2.1 Archival host galaxy observations

An archival spectrum of the host galaxy was available from the Sloan Digital Sky Survey (SDSS; Albareti et al. 2017). The spectrum is displayed in Fig. 1. The lack of common emission lines such as Hα and [O II], combined with strong Balmer absorptions, indicate that this is a quiescent, Balmer-strong galaxy, otherwise known as a post-starburst or E+A galaxy (i.e. an elliptical galaxy showing absorption lines from A-type star atmospheres). TDEs are overrepresented in such galaxies by a factor of 30–35 (Arcavi et al. 2014; French, Arcavi & Zabludoff 2016; Graur et al. 2018), possibly because these galaxies have higher central stellar densities than the background population (Law-Smith et al. 2017; Graur et al. 2018). A stellar population synthesis model is fit to archival host photometry in Gomez et al. (2020).

2.2 Spectroscopy

Follow-up spectra were obtained via the extended Public ESO Spectroscopic Survey of Transient Objects (ePESSTO/ePESSTO+; Smartt et al. 2015) with EFOSC2 on the 3.6-m New Technology Telescope (NTT) at the La Silla Observatory, Chile. A slit width of 1.0 or 1.5 arcsec, depending on seeing, was placed on the target at the parallactic angle. Spectra were reduced and calibrated with standard IRAF routines via the PESSTO pipeline (Smartt et al. 2015). Flux calibration was achieved using standard star observations obtained on the same nights.

Las Cumbres spectra were taken with the FLOYDS spectrographs mounted on the 2-m Faulkes Telescope North and South at Haleakala (USA) and Siding Spring (Australia), respectively. A 2.0- arcsec wide slit was placed on the target at the parallactic angle. One-dimensional

[1] While this paper was under review, another paper on the same event appeared on arXiv by Hung et al. (2020) which we include in our discussions.

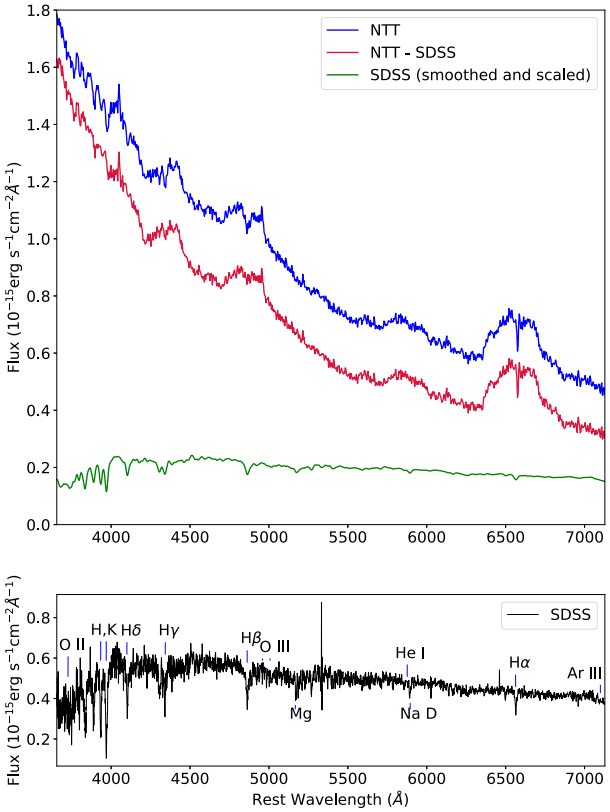

Figure 1. Lower panel: The original SDSS spectrum. Upper panel: (green) the SDSS spectrum degraded to match the resolution and scaled to the slit width of the NTT spectra, (blue) an NTT spectrum from 2018 February 12, and (red) the same NTT spectrum minus the degraded and scaled SDSS spectrum.

spectra were extracted, reduced, and calibrated following standard procedures using the FLOYDS pipeline[2] (Valenti et al. 2014).

Further spectra were taken with the IMACS (Dressler et al. 2011) and LDSS3c spectrographs on the 6.5-m Magellan telescopes, OSMOS on the 2.4-m Hiltner Telescope at MDM observatory (Martini et al. 2011), the Boller and Chivens spectrograph on the Irénée du Pont Telescope and the FAST spectrograph on the 1.5-m Tillinghast Telescope (Fabricant et al. 1998). The spectra were processed using standard IRAF routines with the TWODSPEC package. Bias and flat-field corrections were applied, and the sky background was modelled and subtracted from each image. The one-dimensional spectra were optimally extracted, weighing by the inverse variance of the data. A wavelength calibration was applied using a HeNeAr lamp spectrum taken near the time of each science image. Relative flux calibration was applied to each spectrum using a standard star taken on the same night.

One spectrum was observed with the Intermediate-dispersion Spectrograph and Imaging System (ISIS; Jorden 1990) spectrograph at the William Herschel Telescope (WHT) on 2020 January 6. We used a slit width of 1.0 arcsec in combination with the R600 gratings. The use of a dichroic results in blue and red spectra, covering ∼1400 Å around central wavelengths of 4500 and 7000 Å, respectively. After performing standard data-reduction tasks in IRAF, including a bias subtraction and flat-field normalization, cosmic rays are removed using the LACOS package (van Dokkum, Bloom & Tewes 2012). A wavelength calibration is applied using CuAr+CuNe arc lamp frames; the dispersion in the wavelength solution is <0.1 Å. A summary of all observations is shown in Table A1 in Appendix A.

All spectra up to +206 d after peak were scaled to Las Cumbres photometry, then redshift and extinction corrected using a redshift of $z = 0.045\,73$ and an extinction value of $E(B-V) = 0.0288$ mag (Schlafly & Finkbeiner 2011) in IRAF. We removed host galaxy light by subtracting the archival SDSS spectrum. SDSS spectra have higher resolution (3 Å pixel^{-1}) than a lot of our data (see Table A1). In addition, the host spectrum has a slit width of 3.0 arcsec so had to be scaled to match the slit widths of the other spectra. This was performed by multiplying by the fraction of the host galaxy that would appear in each slit using the galaxy half-light radius of 1 arcsec obtained from SDSS. After correcting for the different slit widths and scaling to SDSS photometry, we subtracted the host galaxy spectrum from our spectra using the SARITH task within IRAF. The host-subtracted spectra were then scaled to host-subtracted photometry from Gomez et al. (2020). This method is illustrated in Fig. 1, while selected host-subtracted NTT spectra are displayed in Fig. 2. We assumed no-host extinction in these subtractions as we see no Sodium absorption. If host extinction is present, it has the effect of dimming AT 2018hyz and making it appear cooler.

We also obtained spectra with the X-shooter spectrograph on the Very Large Telescope (VLT) in slit-nodding mode. X-shooter is an Echelle spectrograph with three arms (UVB, VIS, NIR), with a combined wavelength range from 3200 to 24 700 Å (Vernet et al. 2011). We reduced the spectra with the dedicated ESOREFLEX pipeline (v. 3.3.4). A telluric standard was obtained at a similar airmass to the target, and a telluric spectrum was then generated by dividing the reduced standard spectrum by an interpolated spectrum using the telluric-free regions. The science spectrum was then divided by the residual telluric spectrum to remove these features from the data.

3 SPECTROSCOPIC ANALYSIS

3.1 Host black hole mass

With the high-resolution spectrum from X-shooter displayed in Fig. 3, we were able to accurately measure the host galaxy absorption lines to estimate the central black hole mass via the $M_{\rm BH}-\sigma_\star$ relation. We first resampled the spectrum on to a linear dispersion in the logarithm of wavelength, before normalizing it to the continuum using third-order cubic splines. We masked prominent absorption features, while including TDE emission features to help with comparison to stellar templates.

We then use PPXF (Cappellari 2017) in combination with the Elodie stellar template library (Prugniel & Soubiran 2001; Prugniel et al. 2007) to measure the velocity dispersion using the myriad of stellar absorption features present in the spectrum (see Wevers et al. 2017 for more details). We measure a stellar velocity dispersion of $\sigma_\star = 57 \pm 1$ km s^{-1}; the best-fitting template overlaid on the X-shooter spectrum is inset in Fig. 3. Similar measurements were made using the host SDSS spectrum and our WHT spectrum, giving $\sigma_\star = 59 \pm 3$ and 58 ± 5 km s^{-1}, respectively, consistent with the X-shooter result.

Using the $M_{\rm BH}-\sigma_\star$ relation of McConnell & Ma (2013), the measured velocity dispersion corresponds to a black hole mass of $\log(M_{\rm BH}/{\rm M}_\odot) = 5.25 \pm 0.39$ where the quoted uncertainty includes both the systematic and statistical error. Such a low black hole mass is consistent with the lowest mass black holes in the sample of known TDEs in Wevers et al. (2019a), though we note that our low measurement of σ is significantly out of the range covered by the data used to derive the McConnell & Ma relation. In addition,

[2]https://github.com/svalenti/FLOYDS_pipeline

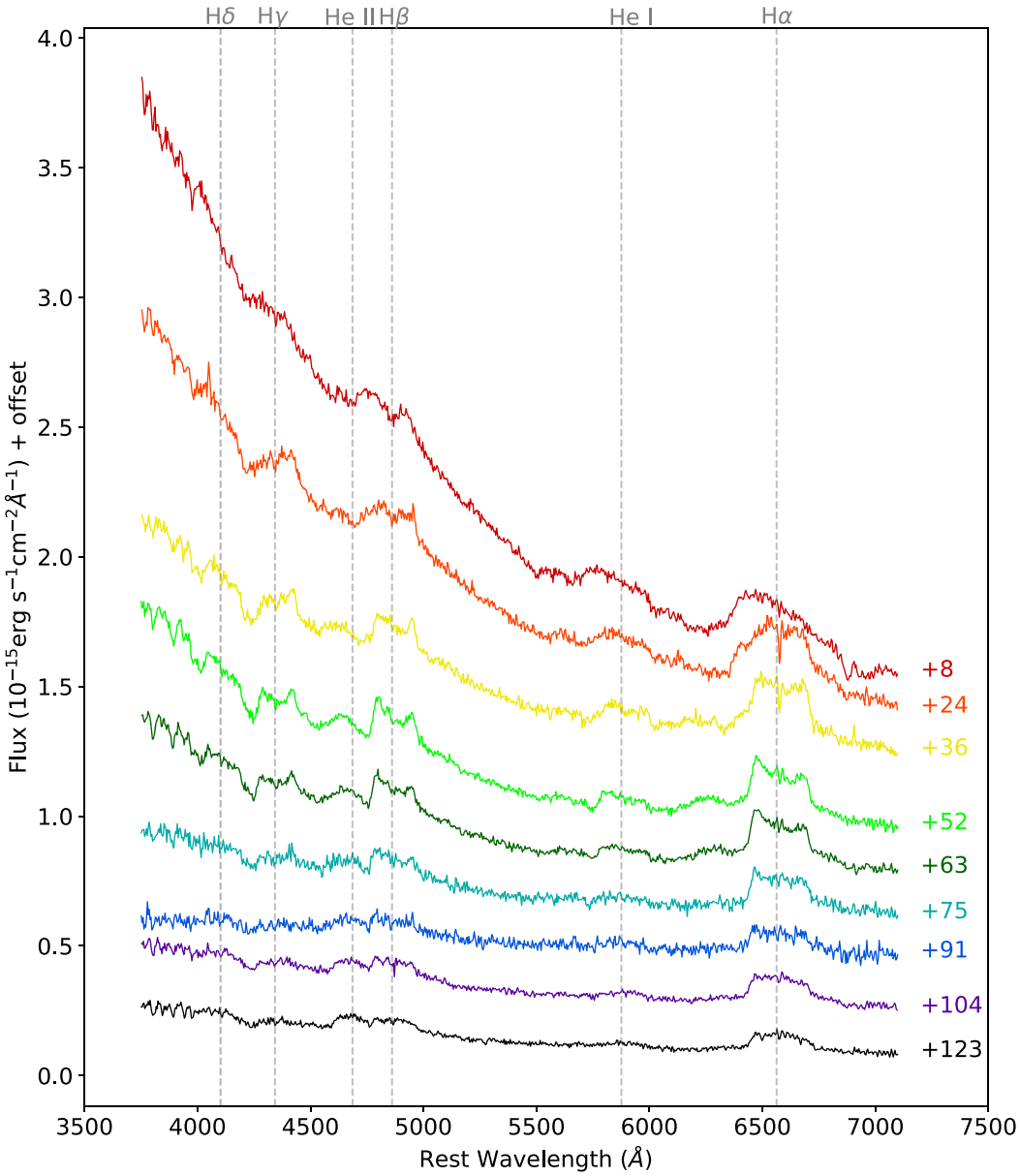

Figure 2. Host-subtracted NTT spectra up to 123 rest-frame days from peak. Features in later spectra are too faint to be visible on this scale. The spectra have been offset for clarity. The number on the right marks how many rest-frame days after peak the spectra were taken.

TDEs typically have an Eddington ratio of 0.1–1 at peak (Wevers et al. 2017; Mockler, Guillochon & Ramirez-Ruiz 2019), whereas the luminosity of AT 2018hyz at peak, 1.9×10^{44} erg s^{-1} (Gomez et al. 2020), would correspond to $\sim 10 L_{\rm Edd}$ for this black hole mass.

If we instead use the $M_{\rm BH}-\sigma_\star$ relation of Kormendy & Ho (2013), we obtain $\log(M_{\rm BH}/{\rm M}_\odot) = 6.09 \pm 0.30$. This is more consistent with the peak luminosity being at $L_{\rm Edd}$. Although this value is closer to what we expect, this relation is derived exclusively for classical elliptical bulges which may or may not apply in this case. Gomez et al. (2020) find $\log(M_{\rm BH}/{\rm M}_\odot) = 6.72 \pm 0.20$ from light-curve modelling, which is higher than we measure from the spectra. Similarly, Hung et al. (2020) measure $\log(M_{\rm BH}/{\rm M}_\odot) = 6.55^{+0.17}_{-0.13}$ from light-curve modelling and $\log(M_{\rm BH}/{\rm M}_\odot) = 6.2$ from a different $M_{\rm BH}-\sigma_\star$ relation. They are in agreement that the McConnell & Ma (2013) relation gives an improbably low mass. We add a further mass estimate using the $M_{\rm BH}-M_{\rm bulge}$ relation from McConnell & Ma (2013). Mendel et al. (2014) find a bulge mass of $\log(M_{\rm bulge}/M_\odot) \sim 8.8$, which gives a black hole mass of $\log(M_{\rm BH}/{\rm M}_\odot) \sim 6.2$ consistent with our other estimates. As it is not clear which measurement should be favoured, it seems reasonable to assume a black hole mass of $10^6\,{\rm M}_\odot$ for the rest of this analysis, with a large uncertainty of a factor of $\gtrsim$2, which gives a peak Eddington ratio of $\sim$1.5.

3.2 Transient line evolution

The spectra of AT 2018hyz are dominated by a blue continuum. Gomez et al. (2020) measure the blackbody continuum temperature from photometry, which drops from an initial temperature of $\sim$22 000 to 16 000 K after 50 d, before rising back up to 21 000 K. To isolate and study the spectral line evolution, we first removed this continuum. To produce the spectra shown in Fig. 4, the continua were fit using fourth-order polynomials with the IRAF CONTINUUM

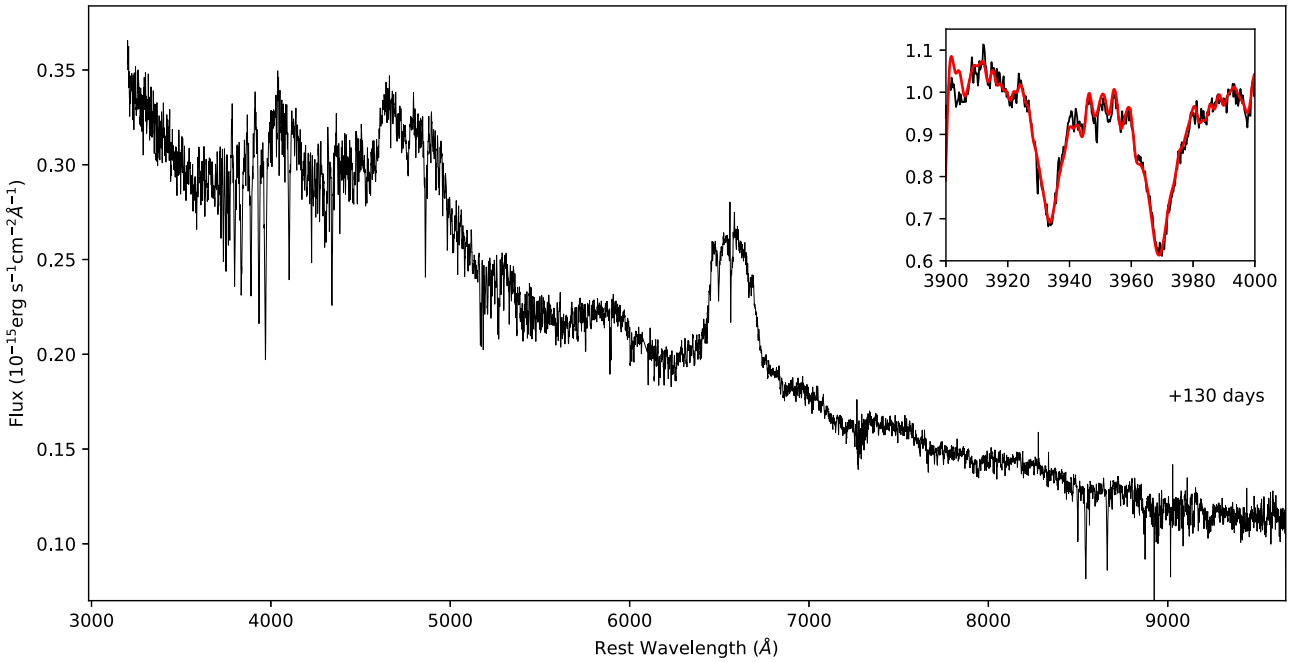

Figure 3. The X-Shooter spectrum of AT 2018hyz. Insert: The normalized X-Shooter spectrum (black) zoomed in on Calcium H and K absorption lines. The best-fitting model is overlaid in red.

package, before being subtracted from the spectra. The subtractions are satisfactory for line visualization, but oversubtract at shorter wavelengths especially at earlier times.

The spectra initially show broad Balmer lines and He I λ5876. At around 70–100 d after peak, He II λ4686 appears and increases in strength. The Balmer line profiles are complex and evolve dramatically. The profile is initially roughly Gaussian but slightly boxy and asymmetric. It becomes boxier with time and develops a double-peaked shape ∼40 d after discovery with a stronger blue peak than red, maintaining the asymmetry. The profile loses the double-horned shape around 90 d after discovery, becoming flat topped before rounding off, losing the asymmetry and developing a Gaussian or maybe even a triangular profile. He I is weaker but appears to follow a similar evolution, suggesting it arises from a similar physical region. In some spectra (e.g. phase 24–75), Hγ appears redshifted. This could be the red peak of a double-peaked line, but we would also expect to see the blue peak. It is not clear what the cause of this feature is. We measured the full width at half-maximum (FWHM) of Hα in each spectrum empirically, as a Gaussian does not consistently provide a good fit. The profile narrows over the period of observations from ∼17 000 to ∼10 000 km s^{-1}. If the observed velocity width corresponds to Keplerian rotation of a disc, an FWHM of 17 000 kms $^{-1}$ implies the orbital radius of the emitting material is $R \sim 600\ R_s$, whereas 10 000 km s^{-1} corresponds to a radius of $R \sim 1800\ R_s$ (where R_s is the Schwarzschild radius, which for a 10^6 M$_\odot$ black hole is ∼0.02 au), though these values would be lower for an inclined disc. The initial high velocity is measured before the profile looks disc-like, hence the velocity width may not correspond to a meaningful rotational velocity.

Once the He II line becomes clearly visible, it is well fit by a Gaussian with an FWHM of 7700 km s^{-1}, corresponding to Keplerian rotation at $\sim 3000\ R_s$. However, at +162 d we observe a secondary peak just blueward of He II which could be due to the N III λ4640 line, suggesting the presence of Bowen fluorescence. We fit a double Gaussian, one at 4640 Å and one at 4686 Å, allowing the widths to vary independently. The N III and He II lines are fit by Gaussians with FWHMs of 3800 and 4200 km s^{-1}, respectively. This suggests that, if it is contaminated by Bowen fluorescence, He II originates further out at $\sim 10\,000\ R_s$, assuming the gas is virial. van Velzen et al. (2020) show that TDEs with Bowen lines tend to have blackbody radii smaller than 6×10^{14} cm; the size of the blackbody radius inferred for AT2018hyz by Gomez et al. (2020) is initially 1.3×10^{15} cm suggesting we should not expect Bowen fluorescence in AT 2018hyz. However, the radius shrinks over time and reaches 6×10^{14} cm after ∼100 d, so it may be possible for these lines to form then. The appearance of He II and weakening of Hα is somewhat similar to AT 2017eqx (Nicholl et al. 2019), though in the latter case, He II is always strong and Hα completely disappears. The change in line strengths and their appearance/disappearance suggests that it may be possible for events to transition between the TDE classes (H, He, and Bowen) defined by van Velzen et al. (2020).

Measuring the line flux was not trivial due to blending between neighbouring broad features. To obtain more reliable measurements we used local continuum subtractions. For each of Hα, Hβ, and Hγ, we defined relatively line-free wavelength ranges on each side of the emission profiles. The lower and upper ranges, respectively, were 6100–6400 Å and 6750–7050 Å for Hα, 4470–4550 Å and 5050–5350 Å for Hβ, and 4190–4240 AA and 4470–4550 Å for Hγ. Within these ranges, we randomly selected regions of the spectra and fit a linear continuum, which was subtracted before integrating the line flux. For each line and each spectrum, this process was iterated 1000 times to determine a mean flux and standard deviation, which we take as an estimate of the uncertainty. The regions are highlighted in Fig. 5, where it is clear how difficult it is to select a region with no contamination. As shown in Fig. 6, the Hα, Hβ, and Hγ emission lines decay over time, Hα/Hβ stays at ∼1.5, while Hγ/Hβ drops from ∼0.6 to ∼0.2, though our Hγ measurement is less reliable as it is a weak line in a contaminated region. The line fluxes we measure, in particular Hβ, are dependent on where we define our continuum regions. However, after experimenting with different regions we find

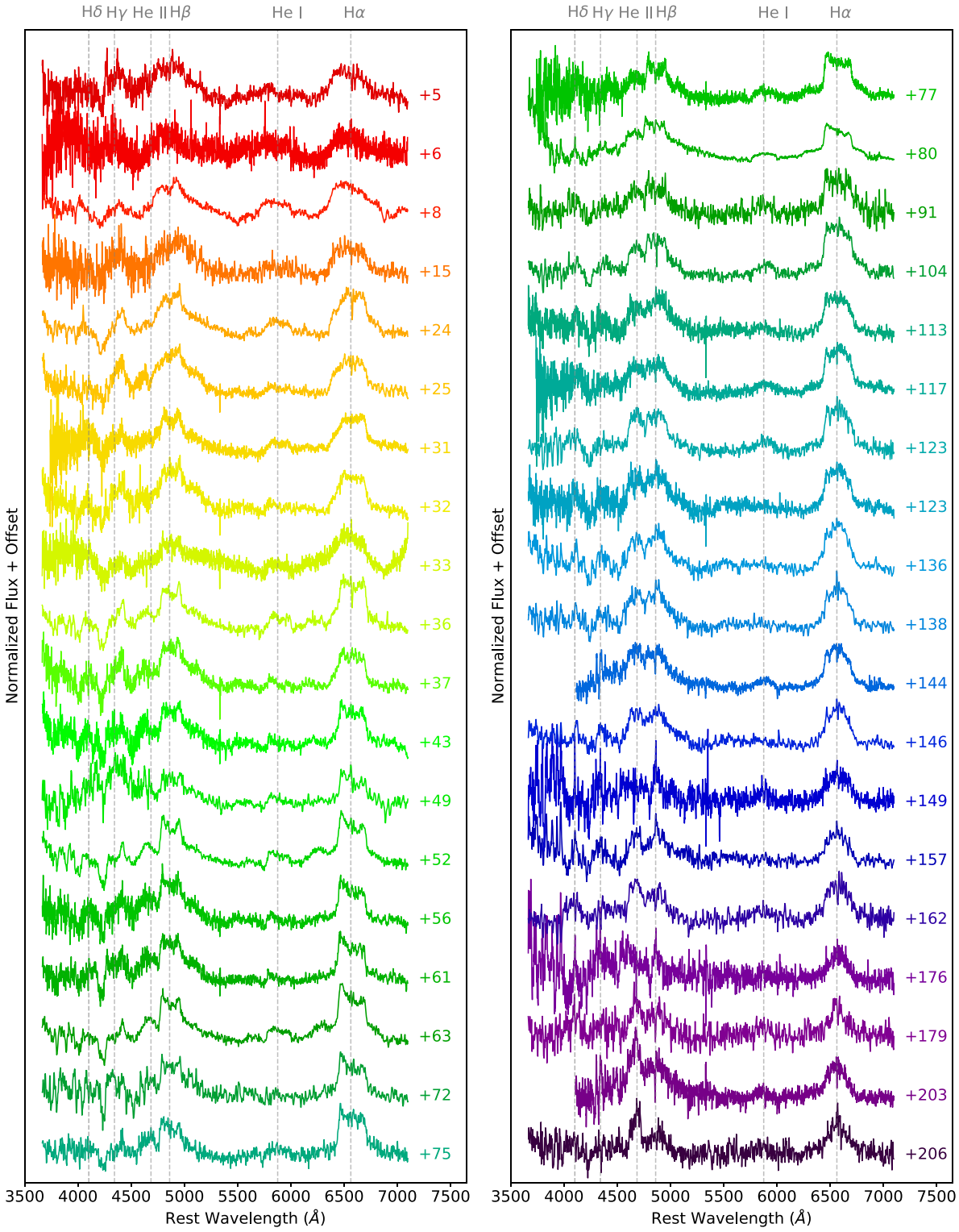

Figure 4. All host and continuum subtracted spectra. The days after peak in the TDE rest frame are marked on the right-hand panel.

Hα/Hβ is always below 2, and any contamination unaccounted for in the Hβ region would mean the true value is lower. The presence of host-extinction would also make the true value of Hα/Hβ lower.

Fig. 7 shows Hα and Hβ in velocity space over six epochs. The two lines show a similar evolution except for the red shoulder on Hβ. We observe a feature appearing at the position of He II 4686 Å at ∼36 d after discovery. A feature also develops blueward of Hα at the same time at around 6300 Å, suggesting it is related to the appearance of the 4686 Å feature.

The order of appearance of the Balmer lines and He II makes sense if we consider the dynamical time-scale, $t_{\rm dyn} = \sqrt{R^3/GM}$. From the velocity width of the Balmer lines, we estimate the emitting region to

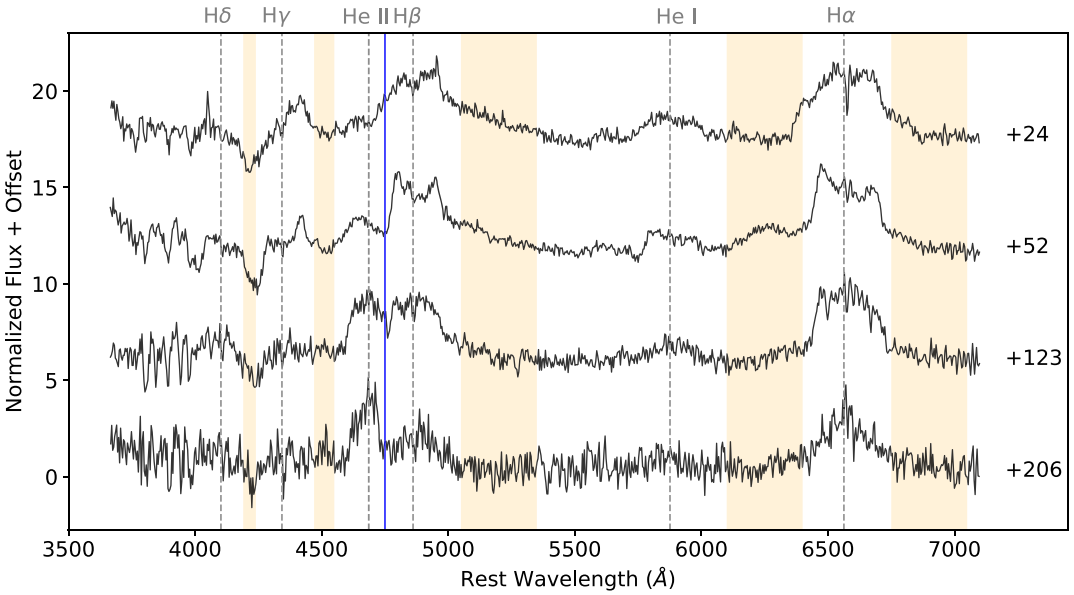

Figure 5. Continuum subtracted spectra from different epochs with emission lines labelled. The time after the peak (in rest-frame days) when each spectrum was taken is marked on the right-hand side. The regions used in local continuum subtractions are highlighted in orange. After continuum subtraction the area between these regions was integrated to find the line flux, with the exception of Hβ, where the lower limit is the solid blue line to avoid He II.

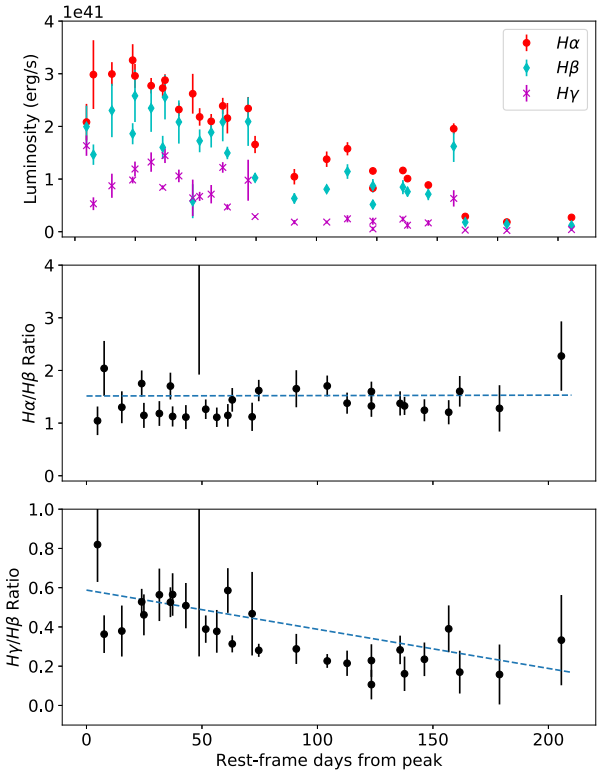

Figure 6. The Hα, Hβ, and Hγ luminosities fade with time (top panel), Hα/Hβ stays roughly constant (middle panel), while Hγ/Hβ appears to decline. The dashed lines show the line of best fit. The error bars are underestimated as they do not include systematics.

initially be at a radius of 600 R_s. For a 10^6 $M_\odot$, black hole this gives a dynamical time-scale of ∼2 d. The radius of the emitting region of the He II line estimated from the linewidth depends on whether or not the Bowen component is present. Assuming pure He II, the emitting region is at 3000 R_s and has a dynamical time-scale of t_{dyn} ∼ 30 d. With the Bowen component the line comes from 10 000 R_s and has t_{dyn} ∼ 160 d. While the ordering of appearance of the lines is consistent with their dynamical time-scales, the appearance of He II after ∼70–100 d is consistent only if the line is at the larger radius, requiring contamination from the Bowen N III line.

After the spectrum 206 rest-frame d from peak, AT 2018hyz became obscured by the Sun. Following its reappearance, we obtained a further two spectra with the NTT, one with the WHT and one with X-Shooter on the VLT. These are displayed in Fig. 8. He II is just visible in the earliest of these and a narrow line has appeared at the position of Hα. At the redshift of AT 2018hyz, Hα falls on a sky line at the edge of the Telluric *B* band, making its veracity uncertain in the NTT spectra. However, the X-Shooter and WHT spectra are of sufficiently high resolution to separate this feature from the telluric band. We subtract the local continuum around the line from the X-Shooter spectrum and fit a two-component Gaussian, displayed in Fig. 9. The broad component is blueshifted by −460 km s^{-1} and has an FWHM of 400 km s^{-1}, while the narrow component is blueshifted by −210 km s^{-1} and has an FWHM of 170 km s^{-1}. However, the line profile is likely affected by host-absorption which we are unable to correct for. The velocity widths of the broad and narrow components correspond to radii of $1.1 \times 10^6 R_S$ and $6.2 \times 10^6 R_S$, respectively. The broad component could be due to [N II] λ6548. It appears redshifted though a feature that could be [N II] λ6584 is also present (see Fig. 9). The most intuitive interpretation of the narrow line is that it is a light echo, produced when photons from the TDE interact with a slow-moving gas cloud at a large radius. One potential effect of this is that our temperature measurements are higher than they should be, as earlier, hotter spectra contribute to later ones (e.g. as in Schmidt et al. 1994). The temperature increase observed after +50 d could be a result of this, however, the narrow line does not appear for around another 200 d so we do not believe the two are related. The light traveltime from the black hole to the radius of the narrow component is ∼700 d. This is consistent with our observations (the line appears some time between our spectra at +206 and +369 d) if the angle

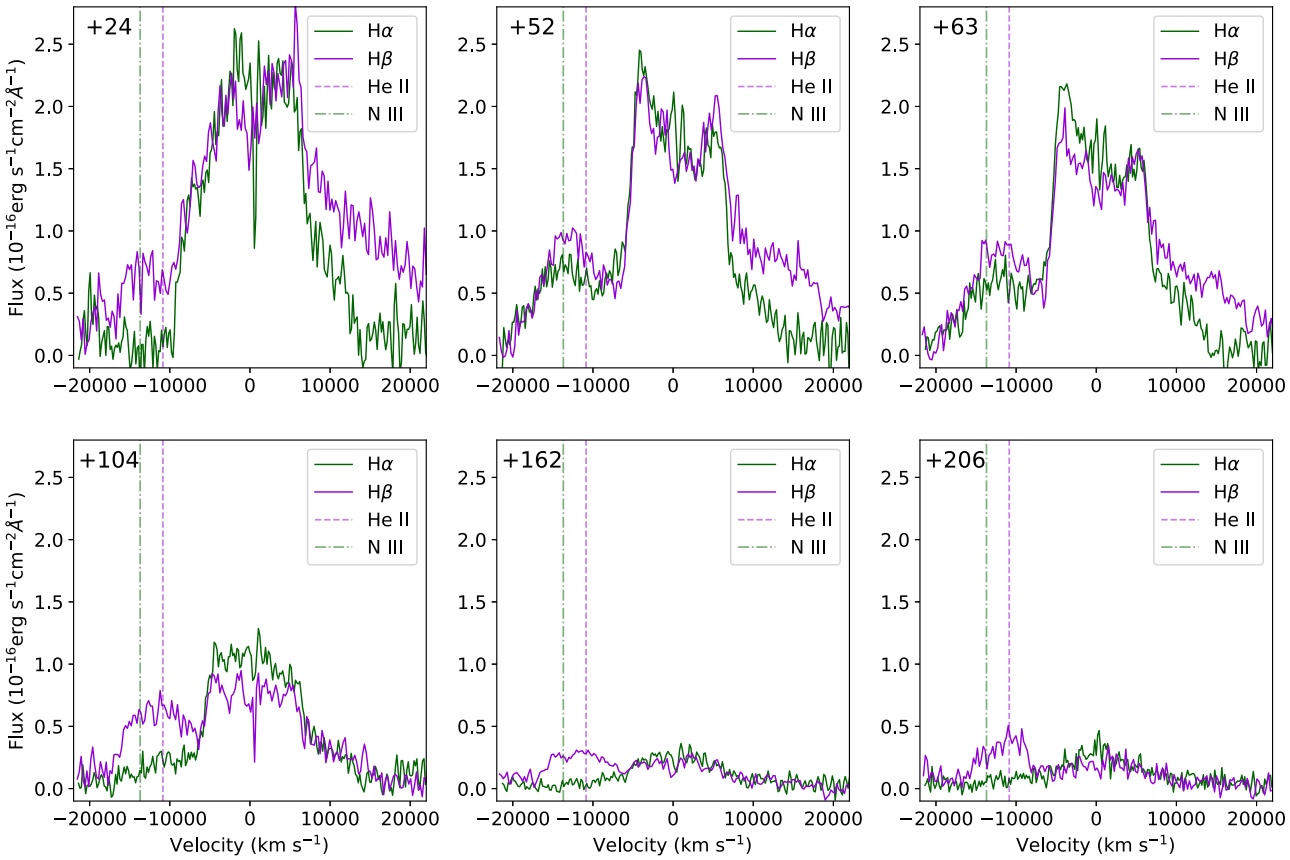

Figure 7. Velocity profiles of Hα and Hβ from six epochs (marked in the top left-hand panel in rest-frame days from peak). At +52 d, the blue bump in Ha is at a similar velocity to what we had assumed to be He II, possibly suggesting a blue-shifted outflow (∼12000 km s^{-1}). At +162 d a second peak appears on He II that matches the position of the N III line produced by Bowen fluorescence.

between gas cloud and line-of-sight to the TDE, from the position of the black hole, is in the range 45° to 60°.

3.3 Disc model fitting

We fit models to the double-peaked emission lines using prescriptions for a circular accretion disc described by Chen & Halpern (1989) and Strateva et al. (2003). We acknowledge that in reality, the scenario would likely be more complex than a circular disc, but the purpose of the fitting is to show that a disc can produce the observed profiles. Initially, we leave four parameters free: the inclination of the disc (i), the power-law index (q) which controls the emission line wing shape where R^{-q} gives the emissivity profile, the inner line emitting radius (e_1) and a local broadening parameter (σ). We keep the outer radius fixed at $2500R_S$ as this has little effect on the resulting line profile. We fit the model to the continuum-subtracted Hα region in the spectrum at +52 d, chosen as it shows a clear double peak. Before fitting the disc model, the bump bluewards of Hα (Section 3.2) was removed by fitting a Gaussian and subtracting. The parameters of the best-fitting models, shown in the top left-hand panel of Fig. 10, are $i = 30.5°$, $q = 3$, $e_1 = 500R_S$, and $\sigma = 747$ km s^{-1}. These best-fitting models also provided good fits to the Hβ emission. We then tried fixing e_1 and q to allow finer grid spacing for i and σ. e_1 was fixed at $500R_S$ as this value consistently fit the line well, and q was set to 1.5 as this value is found observationally in CV discs (Horne & Saar 1991). The fits both look reasonable and support the idea that the double-peaked profiles can be interpreted as evidence of an accretion disc. However, at early and late times (when the Balmer lines do not show the double-peaked profile) the disc model fails to provide a good fit, suggesting that either the emission is being obscured/reprocessed, or the structure of the disc itself is changing. We show how varying different parameters alters the emission-line shape in the remaining panels in Fig. 10.

Hung et al. (2020) perform emission-line fits to multiple epochs using an elliptical disc model combined with a Gaussian component. They find that while the Gaussian component dominates in later epochs, the double-peaked profile is still required for a good fit, suggesting the disc is never completely obscured but that the emission becomes dominated by a radiatively driven wind. The velocity dispersion fit by Hung et al. (2020) is lower than the value we obtain and the inclination is higher, though both are within 2σ of our estimates. This is likely due to the Gaussian component fitting the broader wings thus allowing the disc model to only fit the double peaks. The combination of elliptical disc model and Gaussian component fit the emission lines well, but how much of a contribution the disc component provides at later times is uncertain, and it is possible it completely disappears. Hung et al. (2020) also fit an elliptical model with no Gaussian component and, despite our model being for a circular disc, their best-fitting parameters all agree with ours within 1σ–2σ, suggesting a circular disc is a reasonable approximation.

4 DISCUSSION

4.1 Balmer-line emission

Possibly the most striking result from our observations is the flat Balmer decrement. In a typical AGN BLR, the Hα/Hβ ratio is

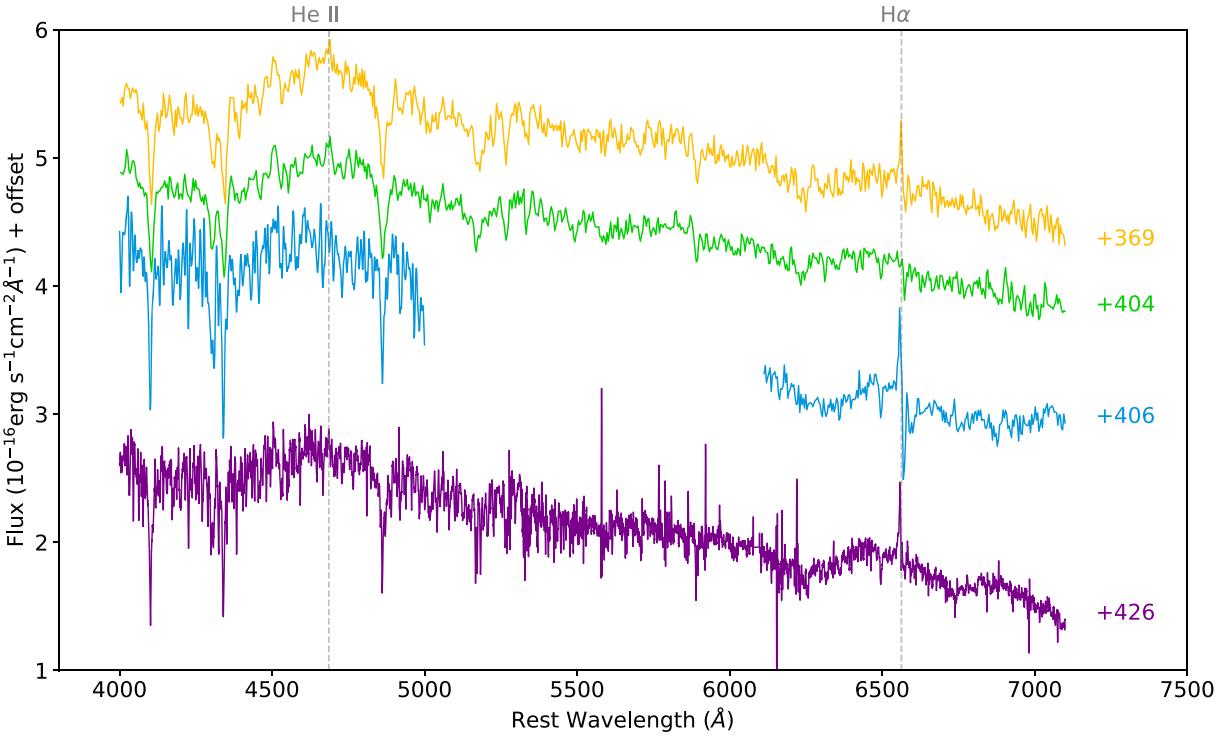

Figure 8. Late-time spectra taken once AT 2018hyz was no longer obscured by the Sun. The first two are from the NTT, the third from the WHT, and the most recent is from X-Shooter. The host has not been subtracted from these spectra. A narrow Hα line has appeared and He II is just visible in the earliest of these spectra.

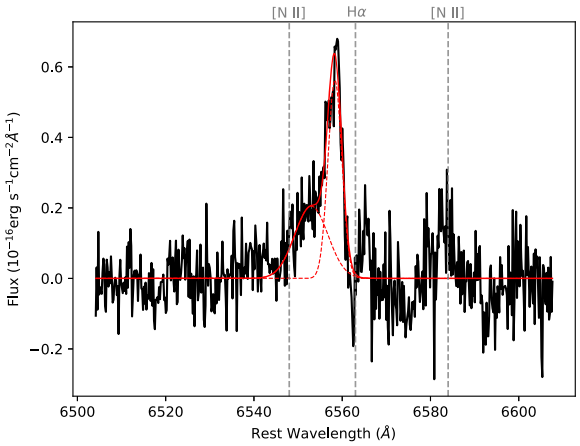

Figure 9. A two Gaussian component fit to the narrow Hα line in the X-Shooter spectrum taken +426 d from peak. The line appears blueshifted, with the narrow component centred on 6558 Å. The broad component might be [N II] λ6548, with the corresponding [N II] λ6584 to the right-hand side.

~3–4, which is consistent with Case B recombination (Osterbrock 1974) combined with reddening, high densities, high-column densities, and an extended ionized continuum (Netzer 2013). Fig. 11 compares ratios expected from Case B to those expected from local thermodynamic equilibrium (LTE). The LTE temperature curves are generated by determining the flux given by a blackbody curve at the position of each emission line, and dividing for the required ratio. The ratios shown by AT 2018hyz are completely inconsistent with Case B but agree with LTE at ~4000 K, suggesting these lines are due to collisional excitation rather than photoionization. The caveat to this temperature measurement is that we have not considered radiative transfer effects, particularly with regards to line saturation (Horne & Marsh 1986). This temperature may therefore be a lower limit.

Low Balmer decrements like this are observed in cataclysmic variables (CVs) and are attributed to thermal emission from an accretion disc chromosphere (Williams 1980). In this scenario, the bulk of the disc is optically thick (thus it looks like a blackbody), while the chromosphere is optically thin in the continuum but thick in the lines. So we see lines from the chromosphere with fluxes corresponding to blackbody emission, superimposed on the blackbody continuum from the disc. As a disc will have both radial and vertical temperature gradients, these blackbodies are not necessarily at the same temperature.

We can test whether the temperature measured from the Balmer-line ratio is consistent with the continuum temperature expected in a disc at that radius. In a simple accretion disc model, the temperature profile of the disc is described by a $T \propto R^{-3/4}$ relation

$$T^4 = \left(\frac{3GM\dot{m}}{8\pi R^3\sigma}\right) = 1.529 \times 10^{22} \left(\frac{L}{L_{\rm Edd}}\right) \left(\frac{M}{10^9\,{\rm M}_\odot}\right)^{-1} \times \left(\frac{R}{R_S}\right)^{-3} \quad (1)$$

Using a black hole mass of $M = 10^6\,{\rm M}_\odot$ and an Eddington ratio of 1.5, then at the initial radius of the Balmer emission, $600R_{\rm S}$, equation (1) gives a temperature of $T = 24\,000$ K, whereas at $1800R_{\rm S}$ (from the narrower lines at later times) we expect $T = 11000$ K. The temperature, we measure from the line ratio is significantly cooler than this, at ~4000 K, but the initial temperature of 24 000 K is consistent with the blackbody continuum temperature measured by Gomez et al. (2020). This suggests our observations cannot be

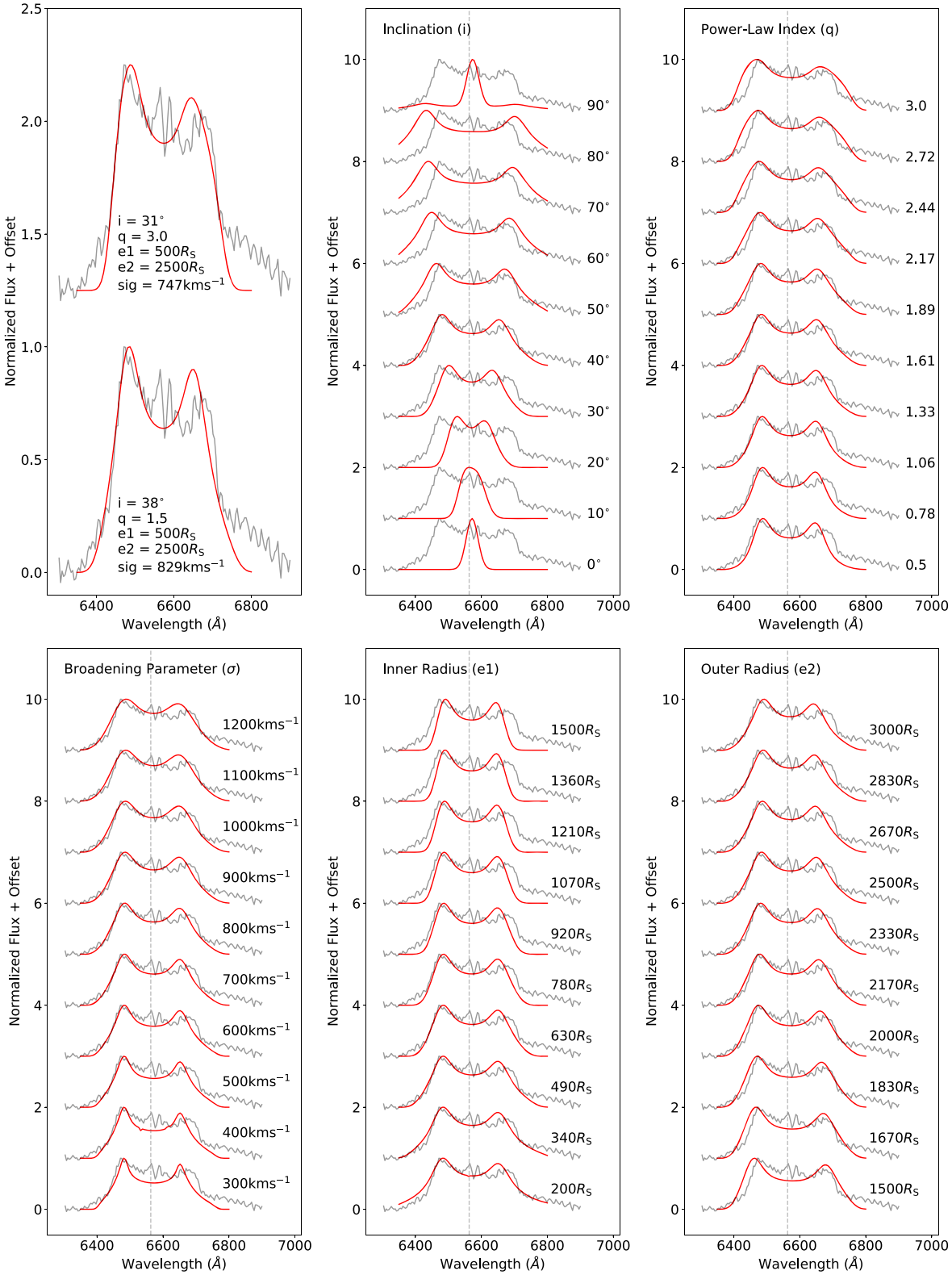

Figure 10. The top left-hand panel shows examples of best-fitting models to our spectrum. The remaining panels explore parameter space of the circular disc model. In each of these plots only one parameter is varied, while the others are fixed at $i = 38°$, $q = 1.5$, $\sigma = 500$ km s^{-1}, $e_1 = 500R_S$, and $e_2 = 2500R_S$.

explained by a single temperature producing both the continuum and lines, which could be explained by a vertical temperature profile.

CV disc models can reproduce flat Balmer decrements but fail to produce He II lines (Williams 1980), suggesting He II lines originate from a different source. It could be that the He II observed in AT 2018hyz originates from another source like debris stream collisions, although then it is not obvious why the line only appears in later spectra. Unlike He II, we observe He I following the same profile

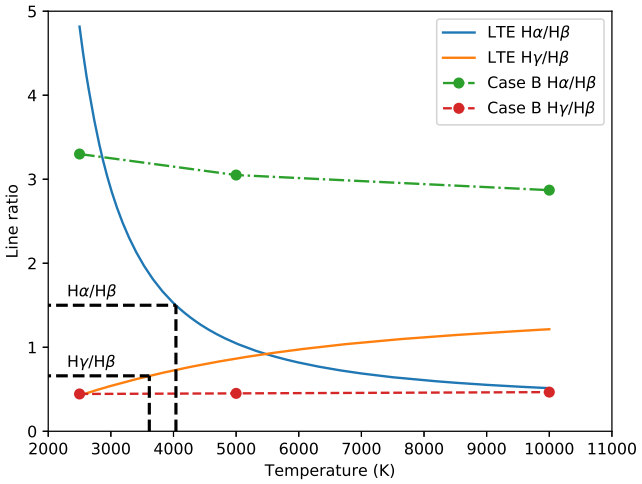

Figure 11. The LTE curve was generated by dividing Hα/Hβ and Hγ/Hβ flux ratios expected from a blackbody at a given temperature. The Case B values are adopted from Osterbrock (1974). The black dashed lines indicate at what temperatures our measured Hα/Hβ and Hγ/Hβ ratios intersect the corresponding LTE curve.

evolution as the Balmer lines, indicating that He I and He II were formed in different parts of the debris.

A disc origin for the Balmer lines is further supported by the double-peaked profiles that develop from ∼40–80 d in both Hα, Hβ, and possibly Hγ. The appearance of these double peaks coincides with a minimum in the blackbody temperature, which subsequently rises again (Gomez et al. 2020). A possible interpretation of the temperature evolution is that there is an initial shock which starts to cool until a disc forms and heats material up again. The blue peak is consistently stronger, which could be a sign of relativistic beaming. From the velocity widths of these lines, we estimated that initially, they originate from a region $\sim 600 R_S$ from the black hole. The tidal radius, $R_t = R_*(M_{BH}/M_*)^{1/3}$, for a 1 $M_\odot$ star around a 10^6 $M_\odot$ black hole is $\sim 25 R_S$. TDE accretion discs are expected to have a radius of order R_t (Rees 1988), whereas the width of the Balmer lines corresponds to a radius of $24 R_t$. However, recent simulations by Bonnerot & Lu (2020) have shown that discs can extend out to tens of R_t, which is more consistent with our measurements. If we instead assume a 0.1-$M_\odot$ star as found by Gomez et al. (2020), $R_t \sim 5 R_S$, so the Balmer linewidths correspond to a radius of $120 R_t$. This is less consistent but not unreasonably so, and we are taking the linewidths at the beginning of observations, possibly before the disc is fully formed. We note that another possible interpretation of the double-peaked lines is that they are produced by an expanding outflow, which can provide blue- and redshifted components as some material moves towards us and some away. This interpretation can explain the ordering of emission line appearance, and can produce the observed temperatures and velocities (Ilya Mandel, private communication). However, we disfavour this interpretation as the receding part of the outflow would be obscured, so it is not obvious how we would observe a red peak. Additional evidence for the disc interpretation comes from a flattening in the UV light curve at ∼550 d after peak (Gomez et al. 2020), which is a sign of late-time accretion (van Velzen et al. 2019b).

In Fig. 4, it is clear that a bump develops around −12 000 km s^{-1} blueward of both Hα and Hβ at +36 d, and remains until at least +80 d. After this, the bump blueward of Hα disappears while the Hβ bump reddens slightly and grows. We suggest that initially, we observe a fast outflow in our line of sight, similar to that described in Prinja & Fullerton (1994). This then fades away, while He II starts to appear at a similar wavelength to the outflow next to Hβ. Another interpretation is that this blue bump is the blue wing of disc emission with smaller radius and larger velocity than the narrower double peaks. The lack of a corresponding red wing could then be due to suppression by strong relativistic beaming. If this is the case, an FWHM of 24 000 km s^{-1} implies emission at $\sim 300 R_S$. The appearance of the blueshifted lines coincides with a plateau in the light curve (Gomez et al. 2020), suggesting these could be related.

The double-peaked profiles that develop in the Balmer lines and possibly in He I only appear temporarily before becoming round-topped again. This is difficult to explain, especially as the constant Hα/Hβ ratio suggests the conditions at the emitting region do not change despite the dramatic evolution in line profile. The changes in the Balmer-line profiles happen over a time consistent with the dynamical time-scale at their estimated radius, meaning the evolving profiles could be due to a change in the structure of the emitting region. It could be that it takes some time for the debris to settle into a disc, at which point we then see defined double peaks, before something happens to disrupt the disc, puffing it up and resulting in rounder line profiles. However, emission-line fitting by Hung et al. (2020) suggests the double-peaks do not completely disappear, but instead the emission becomes dominated by a Gaussian component produced by a radiatively driven wind.

We also observe that the double peaks become less visible around the same time that He II appears, suggesting the disruption of the disc and production of He II could be related. In CVs, it is suspected that He II is produced in the shocked region that forms when material from the donor star collides with the accretion disc. A similar situation could occur in a TDE if some material initially flung far out during the disruption or by shocks in stream–stream collisions eventually falls back and hits the already formed accretion disc. Bonnerot & Lu (2020) find that a constant stream of debris falling on to the accretion disc continually disrupts it and can cause the formation of spiral density waves. The velocity of material crossing the spirals could be altered which is another possible cause of change in the observed emission line profiles, though this is inconsistent with the models fit by Hung et al. (2020).

4.2 He II line emission

The production of He II emission requires a significant flux of EUV photons at wavelengths ≤228 Å. While this is not consistent with the ∼ 16 000–20 000 K temperatures estimated from photometry, Gomez et al. (2020) find weak X-ray emission at $L_X \sim 10^{41}$ergs^{-1} indicating that there is a source of energetic photons. This means that the observed continuum is likely produced via a reprocessing layer. Though the X-ray flux throughout observations remains roughly constant, the plateau in the light curve is more obvious in the UV. The plateau coincides with a rise in the blackbody temperature and may be consistent with the emergence of He II. This could be a sign of a change in the unobservable EUV continuum. Gomez et al. (2020) find that the ratio between host [O III] and X-ray emission is consistent with a weak, preexisting AGN, so further observations are required to determine if this emission is associated with the TDE or not.

There are a number of ways that extended envelopes could form around TDEs. Roth et al. (2016) suggest three possible sources. One is a quasi-static envelope that develops while the accretion disc is forming, though this does not explain why we only see He II at late times. Another option is that while we see Balmer lines formed in a disc, the He II could come from dissipation at large radii. This would

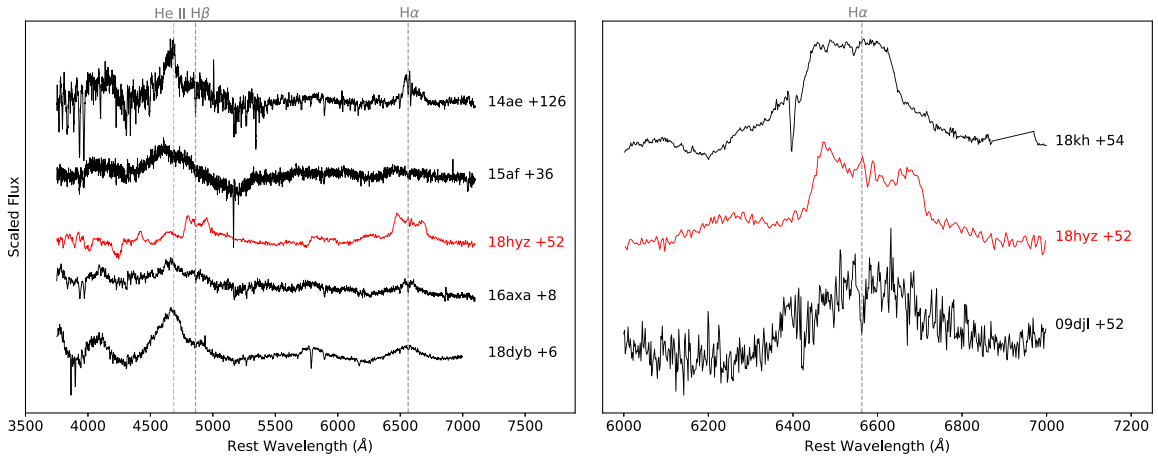

Figure 12. TDE candidates with similar spectral features to AT 2018hyz. Left-hand panel: TDEs with flat Balmer decrements. Also note the late appearing He II in 14ae. Right-hand panel: TDEs which may show disc-like profiles. 18hyz has the most obvious double peak.

explain the difference in line profile between the Balmer and He II lines. The third possibility is an outflow. This could be consistent with the late appearance of He II and be responsible for the increase in temperature. As the outflow expands it reaches the radius at which He II is thermalized, but photoionized Balmer lines are still self-absorbed. We know from reverberation mapping that AGN BLRs are stratified, and He II comes from much closer in than the Balmer lines (Peterson 1993). Metzger & Stone (2016) predict that a continually expanding outflow will eventually result in 'ionization-breakout', at which point X-ray and EUV photons can escape the envelope. This has been observed to occur 200–300 d after the UV/optical peak in other events (Holoien et al. 2016; Liu et al. 2019). The X-ray observations in Gomez et al. (2020) extend to 232 d post-peak but show no sign of re-brightening, and late-time observations at ∼550 d also yield a non-detection.

4.3 Consistency with a unified TDE model

The reprocessing combined with the possible outflow are consistent with the unified TDE models presented by Dai et al. (2018) and Nicholl et al. (2019). In this scenario, an accretion disc forms rapidly within an envelope, and in the polar regions winds can develop. The envelope around the disc can be the origin of the cooler continuum observed in our spectra and trap EUV/X-ray photons. As the polar outflow expands, it reaches the radius from which He II can be produced, as described above. The He II originating from an outflow rather than the envelope allows the late appearance of He II to be consistent with the result found by Gomez et al. (2020) that the envelope is contracting. The observation of He II and blueshifted Balmer lines suggests we are observing the transient somewhat face-on as we must be observing the polar region. The lack of photoionized lines from the envelope would suggest it is compact, as the emission lines are self-absorbed at smaller radii (Roth et al. 2016). A more compact reprocessing layer means the viewing angle into the central engine and outflows is wider. This is consistent with the inclination implied by the disc emission line profile fits.

We suspect that the collisionally excited Balmer lines are from the disc itself. We know the radius of the continuum reprocessing layer is initially $\sim 10^{15}$ cm from SED fits (Gomez et al. 2020) and the widths of the Balmer lines suggest they are being emitted at $\sim 10^{14}$ cm, implying, as expected, that the disc is smaller than the reprocessing layer. The He II width (assuming an N III component in blending) places its emission region at $\sim 3 \times 10^{15}$ cm, outside of the continuum radius. This is consistent with He II arising from an outflow as it expands beyond the reprocessing layer. Gomez et al. (2020) find that the optical depth of the continuum envelope at peak is ∼0.8, but that this increases to 18 at late times. The initial low optical depth may be due to the star only being partially disrupted, and the increase could explain why the Balmer emission lines lose their double peaks, as the emitting region gets more obscured.

4.4 Comparison to other TDE candidates

We searched the literature for other TDE candidates with similar characteristics to AT 2018hyz. The spectra are compared in Fig. 12. PS18kh (Holoien et al. 2019) was a TDE that showed similar line-profile evolution, initially showing roundish profiles that became boxy and possibly double-peaked over time with He II appearing at late times (Hung et al. 2019). It had a peak luminosity of $L = 9.8 \times 10^{43}$ erg s^{-1} and emitted a total energy $E = 3.82 \times 10^{50}$ erg over the observing period, similar to values measured for AT 2018hyz (Gomez et al. 2020). The temperature was similar at first, ranging from 14 000 to 22 000 K, but at 250 d after peak it had increased to $T \gtrsim 50\,000$K (van Velzen et al. 2019a). Also, unlike AT 2018hyz the Balmer ratio in PS18kh is consistent with recombination, though this could be affected by reddening. Holoien et al. (2019) fit elliptical disc models to the Hα line profiles of PS18kh, finding a good fit to an evolving disc. However, Hung et al. (2019) find good fits to a spherical outflow model, arguing the double-peaked shape is due to residuals from the host galaxy subtraction. In the case of AT 2018hyz, the double peaks are much more obvious and robust against host removal.

PTF09djl showed double-peaked Hα emission with one peak centred on the rest wavelength and the second redshfited by 3.4×10^4 km s^{-1} (Arcavi et al. 2014). Disc models fit to these lines by Arcavi et al. (2014) required a bulk motion of 1.5×10^4 km s^{-1} to account for the redshifted second peak, although Liu et al. (2017) successfully fit a disc model with a high eccentricity at large inclination.

ASASSN-14ae (Holoien et al. 2014) is similar in that it initially only showed broad Balmer and He I emission lines with He II appearing at a later epoch. We measured the Balmer ratio of an ASASSN-14ae spectrum taken 37 d after discovery applying the same method we have used with our AT 2018hyz spectra. We obtain

a value Hα/Hβ = 1.8 ± 0.5, which could suggest this TDE also produced collisional lines, though this was performed without host subtraction. Leloudas et al. (2019) found a similarly low Balmer decrement in the TDE candidate AT 2018dyb, as well as in two other TDE candidates, iPTF15af and iPTF16axa (Hung et al. 2017; Blagorodnova et al. 2019). This suggests collisional lines may not be unusual in TDEs, and it should not be assumed that lines are always produced by photoionization and recombination.

5 CONCLUSION

We have presented one of the best sampled spectroscopic data sets of a TDE to date (in addition to the well-sampled light curve in Gomez et al. 2020), showing AT 2018hyz to be a strong TDE candidate with complex line evolution and revealing convincing evidence of disc formation. Measurements of velocity dispersion suggest a host black hole mass in the region of 10^6 M$_\odot$, consistent with emission at $\sim L_{\rm Edd}$ at peak, similar to other TDEs.

The spectra initially show a strong, blue continuum with broad, but weak, He I, and Balmer lines. Over time the blue continuum and broad lines fade but He II appears, showing the evolution from an H- to He-strong TDE. The Balmer lines initially have velocity widths of 17 000 km s^{-1}, which narrow to 10 000 km s^{-1}, corresponding to Keplerian motion in regions 600 to 1800$R_{\rm S}$ from the black hole, respectively. The He II line has a width of 7700 km s^{-1}, which places its emission at 3000$R_{\rm S}$. However, including a contribution from N III λ4640, a line produced by Bowen fluorescence, would mean He II is narrower and actually comes from a region at 10 000$R_{\rm S}$. In either case, He II comes from a larger radius than the Balmer emission, consistent with its later appearance if the line-emitting region forms dynamically.

We measure a constant ratio Hα/Hβ ∼1.5 during the period of observations. Such a low ratio suggests emission from a region in LTE which is optically thin to continuum but thick to lines. Such conditions are seen in disc chromospheres in CVs. The resemblance to CVs is strengthened by the fact that He II seems to be produced in a different region to the Balmer lines.

The double-peaked profiles that develop in the Balmer lines and possibly He I are further evidence that the emission originates from an accretion disc around the black hole. The fact that the double peaks only appear temporarily before fading away again is difficult to explain. The time-scale over which changes in the line profiles occur is consistent with the dynamical time-scale at the radius associated with the Balmer lines, so the observed line evolution could be due to structural changes in the disc. However, the observed increase in optical depth suggests that obscuration may be the cause of the changing profiles. The initial low optical depth of the continuum envelope due to the possible partial disruption may be the reason we are able to see through to these double-peaked lines at all. Emission-line fitting by Hung et al. (2020) suggests the double peaks do not completely fade away, but emission becomes wind-dominated at alter times. This disfavours a change in the disc structure being the mechanism behind the line profile evolution.

The late-emerging He II could be explained by an outflow extending beyond the continuum emitting region that only reaches the radius required to produce He II at late times. This combined with the blueshifted Balmer lines and X-ray detections are consistent with TDE unification models in which many TDEs may produce similar conditions, but what is observed depends on viewing angle. In the case of AT 2018hyz we must have a view close enough to the polar region to see some outflow and X-rays, but close enough to edge-on to still see double-peaked lines. This rather specific sight line might explain why we have not seen quite the same spectral evolution in any other TDEs.

AT 2018hyz exhibits perhaps the clearest double-peaked emission lines that have been observed in a TDE and provides strong observational evidence that accretion discs form in at least some TDEs and are a significant source of the observed luminosity. However, disc profiles were only visible in the emission lines for a short period during the evolution of AT 2018hyz, showing the need for high-cadence spectroscopic follow-up of TDEs. As we move into the era of large TDE samples with current (ZTF; van Velzen et al. 2019a) and future surveys (LSST), dedicated spectroscopic observations will be crucial to unveiling the physical processes occurring in these events.

ACKNOWLEDGEMENTS

We thank I. Mandel for insightful comments and suggestions. We thank Y. Beletsky for carrying out the Magellan observations. PS is supported by a Science & Technology Facilities Council (STFC) studentship. MN is supported by a Royal Astronomical Society Research Fellowship. GL was supported by a research grant (19054) from VILLUM FONDEN. IA is a CIFAR Azrieli Global Scholar in the Gravity and the Extreme Universe Program and acknowledges support from that program, from the Israel Science Foundation (grant numbers 2108/18 and 2752/19), from the United States – Israel Binational Science Foundation (BSF), and from the Israeli Council for Higher Education Alon Fellowship. TW is funded in part by European Research Council grant 320360 and by European Commission grant 730980. JB and DAH are supported by NASA grant 80NSSC18K0577. NCS acknowledges support by the Science and Technology Facilities Council (STFC), and from STFC grant ST/M001326/1. KH acknowledges support from STFC grant ST/R000824/1. MG is supported by the Polish NCN MAESTRO grant 2014/14/A/ST9/00121. NI was partially supported by Polish NCN DAINA grant No. 2017/27/L/ST9/03221. LG was funded by the European Union's Horizon 2020 research and innovation programme under the Marie Skłodowska-Curie grant agreement No. 839090. KM acknowledges support from ERC Starting Grant grant no. 758638. FO acknowledge the support of the H2020 European HEMERA program, grant agreement No 730970. TEMB was funded by the CONICYTPFCHA/DOCTORADOBECAS CHILE/2017-72180113. This work is based on observations collected at the European Organisation for Astronomical Research in the Southern Hemisphere under ESO programmes 1103.D-0328 and 0104.B-0709 and as part of ePESSTO (the Public ESO Spectroscopic Survey for Transient Objects Survey); observations from the Las Cumbres network; data gathered with the 6.5 meter Magellan Telescopes located at Las Campanas Observatory, Chile; observations obtained at the MDM Observatory, operated by Dartmouth College, Columbia University, Ohio State University, Ohio University, and the University of Michigan; service-mode observations (proposal ID: SW2019/P7) made with the WHT operated on the island of La Palma by the Isaac Newton Group of Telescopes in the Spanish Observatorio del Roque de los Muchachos of the Instituto de Astrofísica de Canarias. This research has made use of the NASA/ IPAC Infrared Science Archive, which is operated by the Jet Propulsion Laboratory, California Institute of Technology, under contract with the National Aeronautics and Space Administration.

DATA AVAILABILITY

All data will be made public via WISeREP and the Open TDE Catalog immediately upon acceptance.

REFERENCES

Albareti F. D. et al., 2017, ApJS, 233, 25
Arcavi I. et al., 2014, ApJ, 793, 38
Auchettl K., Guillochon J., Ramirez-Ruiz E., 2017, ApJ, 838, 149
Blagorodnova N. et al., 2019, ApJ, 873, 92
Bonnerot C., Lu W., 2020, MNRAS, 495, 1374
Bonnerot C., Rossi E. M., Lodato G., 2017, MNRAS, 464, 2816
Brimacombe J., Stanek K. Z., 2018, Transient Name Server Discovery Report 2018-1708, 1
Cappellari M., 2017, MNRAS, 466, 798
Chen K., Halpern J. P., 1989, ApJ, 344, 115
Dai L., McKinney J. C., Roth N., Ramirez-Ruiz E., Miller M. C., 2018, ApJ, 859, L20
Dong S., Bose S., Chen P., Brink T. G., de Jaeger T., Filippenko A. V., Zheng W., 2018, Astron. Telegram, 12198, 1
Dressler A. et al., 2011, PASP, 123, 288
Fabricant D., Cheimets P., Caldwell N., Geary J., 1998, PASP, 110, 79
French K. D., Arcavi I., Zabludoff A., 2016, ApJ, 818, L21
Gezari S. et al., 2012, Nature, 485, 217
Gezari S., Cenko S. B., Arcavi I., 2017, ApJ, 851, L47
Gomez S. et al., 2020, MNRAS, 497, 1925
Graur O., French K. D., Zahid H. J., Guillochon J., Mandel K. S., Auchettl K., Zabludoff A. I., 2018, ApJ, 853, 39
Guillochon J., Manukian H., Ramirez-Ruiz E., 2014, ApJ, 783, 23
Hills J. G., 1975, Nature, 254, 295
Hinshaw G. et al., 2013, ApJS, 208, 19
Holoien T. W. S. et al., 2014, MNRAS, 445, 3263
Holoien T. W. S. et al., 2016, MNRAS, 463, 3813
Holoien T. W. S. et al., 2019, ApJ, 880, 120
Horne K., Marsh T. R., 1986, MNRAS, 218, 761
Horne K., Saar S. H., 1991, ApJ, 374, L55
Hung T. et al., 2017, ApJ, 842, 29
Hung T. et al., 2019, ApJ, 879, 119
Hung T. et al., 2020, preprint (arXiv:2003.09427)
Jiang Y.-F., Guillochon J., Loeb A., 2016, ApJ, 830, 125
Jorden P. R., 1990, in Crawford D. L., ed., Proc. SPIE Conf. Ser. Vol. 1235, Instrumentation in Astronomy VII. SPIE, Bellingham, p. 790
Kochanek C. S. et al., 2017, PASP, 129, 104502
Komossa S., 2017, Astron. Nachr., 338, 256
Kormendy J., Ho L. C., 2013, ARA&A, 51, 511
Law-Smith J., Ramirez-Ruiz E., Ellison S. L., Foley R. J., 2017, ApJ, 850, 22
Lawrence A., 2012, MNRAS, 423, 451
Leloudas G. et al., 2019, ApJ, 887, 218
Liu F. K., Zhou Z. Q., Cao R., Ho L. C., Komossa S., 2017, MNRAS, 472, L99
Liu X.-L., Dou L.-M., Shen R.-F., Chen J.-H., 2019, preprint (arXiv:1912.06081)
McConnell N. J., Ma C.-P., 2013, ApJ, 764, 184
Martini P. et al., 2011, PASP, 123, 187
Mendel J. T., Simard L., Palmer M., Ellison S. L., Patton D. R., 2014, ApJS, 210, 3
Metzger B. D., Stone N. C., 2016, MNRAS, 461, 948
Mockler B., Guillochon J., Ramirez-Ruiz E., 2019, ApJ, 872, 151
Netzer H., 2013, The Physics and Evolution of Active Galactic Nuclei. Cambridge Univ. Press, Cambridge
Nicholl M. et al., 2019, MNRAS, 488, 1878
Onori F. et al., 2019, MNRAS, 489, 1463
Osterbrock D. E., 1974, Astrophysics of Gaseous Nebulae, 1 edn. W. H. Freeman and Co., San Francisco, p. 69
Peterson B. M., 1993, PASP, 105, 247
Phinney E. S., 1989, in Morris M., ed., IAU Symp. Vol. 136, The Center of the Galaxy. Kluwer, Dordrecht, p. 543
Piran T., Svirski G., Krolik J., Cheng R. M., Shiokawa H., 2015, ApJ, 806, 164
Prinja R. K., Fullerton A. W., 1994, Ap&SS, 221, 67
Prugniel P., Soubiran C., 2001, A&A, 369, 1048
Prugniel P., Soubiran C., Koleva M., Le Borgne D., 2007, preprint (arXiv:astro-ph/0703658)
Rees M. J., 1988, Nature, 333, 523
Roth N., Kasen D., Guillochon J., Ramirez-Ruiz E., 2016, ApJ, 827, 3
Schlafly E. F., Finkbeiner D. P., 2011, ApJ, 737, 103
Schmidt B. P., Kirshner R. P., Leibundgut B., Wells L. A., Porter A. C., Ruiz-Lapuente P., Challis P., Filippenko A. V., 1994, ApJ, 434, L19
Shappee B. J. et al., 2014, ApJ, 788, 48
Shiokawa H., Krolik J. H., Cheng R. M., Piran T., Noble S. C., 2015, ApJ, 804, 85
Smartt S. J. et al., 2015, A&A, 579, A40
Strateva I. V. et al., 2003, AJ, 126, 1720
Strubbe L. E., Quataert E., 2009, MNRAS, 400, 2070
Svirski G., Piran T., Krolik J., 2017, MNRAS, 467, 1426
Valenti S. et al., 2014, MNRAS, 438, L101
van Dokkum P. G., Bloom J., Tewes M., 2012, Astrophysics Source Code Library, record ascl:1207.005
van Velzen S. et al., 2019a, ApJ, 872, 198
van Velzen S., Stone N. C., Metzger B. D., Gezari S., Brown T. M., Fruchter A. S., 2019b, ApJ, 878, 82
van Velzen S. et al., 2020, preprint (arXiv:2001.01409)
Vernet J. et al., 2011, A&A, 536, A105
Wevers T., van Velzen S., Jonker P. G., Stone N. C., Hung T., Onori F., Gezari S., Blagorodnova N., 2017, MNRAS, 471, 1694
Wevers T. et al., 2019a, MNRAS, 487, 4136
Wevers T. et al., 2019b, MNRAS, 488, 4816
Williams R. E., 1980, ApJ, 235, 939

APPENDIX A: TABLE OF OBSERVATIONS

Table A1. Summary of all observations used in this paper. X-Shooter setup shown is for VIS arm. For UVB arm: exp time = 1360 s, FWHM = 0.80 Å, and slit width = 1.0 arcsec. For NIR arm: exp time = 13 × 100 s, FWHM = 3.1 Å, and slit width = 0.9 arcsec.

UT Date	MJD	Phase (days from peak)	Exposure time (s)	Airmass (start of obs)	Telescope + Instrument	FWHM (Å)	Slit width (arcsec)
2018 Nov 12	58434	+5	2700	1.73	OGG 2m+FLOYDS	12	2.00
2018 Nov 13	58435	+6	2100	1.23	Tillinghast+FAST	3.8	3.00
2018 Nov 15	58437	+8	1500	1.64	NTT+EFOSC2	16	1.00
2018 Nov 23	58445	+15	2700	1.50	OGG 2m+FLOYDS	12	2.00
2018 Dec 2	58454	+24	1500	1.71	NTT+EFOSC2	16	1.00
2018 Dec 3	58455	+25	2700	1.17	OGG 2m+FLOYDS	12	2.00
2018 Dec 9	58461	+31	7200	1.20	MDM+OSMOS	6.0	1.00
2018 Dec 10	58462	+32	2700	1.07	OGG 2m+FLOYDS	12	2.00
2018 Dec 11	58463	+33	1800	1.15	Tillinghast+FAST	3.8	3.00
2018 Dec 15	58467	+36	1500	1.78	NTT+EFOSC2	16	1.00

Table A1 – *continued*

UT Date	MJD	Phase (days from peak)	Exposure time (s)	Airmass (start of obs)	Telescope + Instrument	FWHM (Å)	Slit width (arcsec)
2018 Dec 16	58468	+37	2700	1.07	OGG 2m+FLOYDS	12	2.00
2018 Dec 22	58474	+43	2700	1.08	OGG 2m+FLOYDS	12	2.00
2018 Dec 28	58480	+49	2700	1.77	COJ 2m+FLOYDS	12	2.00
2018 Dec 31	58483	+52	1800	1.17	NTT+EFOSC2	16	1.00
2019 Jan 5	58488	+56	2700	1.23	OGG 2m+FLOYDS	12	2.00
2019 Jan 10	58493	+61	3600	1.16	OGG 2m+FLOYDS	12	2.00
2019 Jan 12	58495	+63	1500	1.17	NTT+EFOSC2	16	1.00
2019 Jan 21	58504	+72	3600	1.26	OGG 2m+FLOYDS	12	2.00
2019 Jan 24	58507	+75	1500	1.17	NTT+EFOSC2	16	1.00
2019 Jan 27	58510	+77	7200	1.22	MDM+OSMOS	6.0	1.00
2019 Jan 30	58513	+80	1800	1.22	Clay+LDSS3c	4.3	1.00
2019 Feb 10	58524	+91	1500	1.30	NTT+EFOSC2	16	1.00
2019 Feb 24	58538	+104	1800	1.38	NTT+EFOSC2	16	1.00
2019 Mar 5	58547	+113	3600	1.52	OGG 2m+FLOYDS	12	2.00
2019 Mar 9	58551	+117	7200	1.20	MDM+OSMOS	6.0	1.00
2019 Mar 16	58558	+123	3600	1.15	OGG 2m+FLOYDS	12	2.00
2019 Mar 16	58558	+123	2 × 1800	1.20 + 1.17	NTT+EFOSC2	16	1.00
2019 Mar 23	58565	+130	920	1.18	VLT+X-SHOOTER	0.88	0.90
2019 Mar 29	58571	+136	3600	1.07	OGG 2m+FLOYDS	12	2.00
2019 Mar 31	58573	+138	1800	1.08	OGG 2m+FLOYDS	12	2.00
2019 Apr 7	58580	+144	3600	1.66	Baade+IMACS	4.0	1.00
2019 Apr 09	58582	+146	3600	1.11	OGG 2m+FLOYDS	12	2.00
2019 Apr 12	58585	+149	900	1.16	IdP+B&C	2.0	1.65
2019 Apr 20	58593	+157	3600	1.08	OGG 2m+FLOYDS	12	2.00
2019 Apr 25	58598	+162	2 × 2700	1.50 + 1.89	NTT+EFOSC2	16	1.00
2019 May 10	58613	+176	900	1.18	IdP+B&C	2.0	1.65
2019 May 13	58616	+179	2700	1.76	NTT+EFOSC2	16	1.00
2019 Jun 07	58641	+203	2400	1.66	Baade+IMACS	4.0	1.00
2019 Jun 10	58644	+206	3600	1.33	NTT+EFOSC2	16	1.50
2019 Nov 28	58815	+369	2 × 2700	1.80 + 1.61	NTT+EFOSC2	16	1.00
2020 Jan 3	58851	+404	2 × 2700	1.17 + 1.18	NTT+EFOSC2	16	1.00
2020 Jan 6	58854	+406	2700	1.12	WHT+ISIS	1.6	1.00
2020 Jan 26	58874	+426	1300	1.22	VLT+X-SHOOTER	0.88	0.90

[1]*Institute for Astronomy, University of Edinburgh, Royal Observatory, Blackford Hill, Edinburgh EH9 3HJ, UK*
[2]*Birmingham Institute for Gravitational Wave Astronomy and School of Physics and Astronomy, University of Birmingham, Birmingham B15 2TT, UK*
[3]*Center for Astrophysics | Harvard & Smithsonian, 60 Garden Street, Cambridge, MA 02138-1516, USA*
[4]*The School of Physics and Astronomy, Tel Aviv University, Tel Aviv 69978, Israel*
[5]*CIFAR Azrieli Global Scholars program, CIFAR, Toronto M5G 1M1, Canada*
[6]*Institute of Astronomy, University of Cambridge, Madingley Road, Cambridge CB3 0HA, UK*
[7]*DTU Space, National Space Institute, Technical University of Denmark, Elektrovej 327, DK-2800 Kgs. Lyngby, Denmark*
[8]*Department of Particle Physics and Astrophysics, Weizmann Institute of Science, 234 Herzl St, 76100 Rehovot, Israel*
[9]*European Southern Observatory, Alonso de Córdova 3107, Casilla 19, Santiago, Chile*
[10]*Center for Interdisciplinary Exploration and Research in Astrophysics and Department of Physics and Astronomy, Northwestern University, 2145 Sheridan Road, Evanston, IL 60208-3112, USA*
[11]*Department of Physics, University of California, Santa Barbara, CA 93106-9530, USA*
[12]*Las Cumbres Observatory, 6740 Cortona Dr, Suite 102, Goleta, CA 93117-5575, USA*
[13]*School of Physics and Astronomy, University of Southampton, Southampton SO17 1BJ, UK*
[14]*Astrophysical Institute, Department of Physics and Astronomy, 251B Clippinger Lab, Ohio University, Athens, OH 45701-2942, USA*
[15]*Departamento de Física Teórica y del Cosmos, Universidad de Granada, E-18071 Granada, Spain*
[16]*Astronomical Observatory, University of Warsaw, Al. Ujazdowskie 4, PL-00-478 Warszawa, Poland*
[17]*University of St Andrews, SUPA School of Physics & Astronomy, North Haugh, St Andrews KY16 9SS, UK*
[18]*School of Physics & Astronomy, Cardiff University, Queens Buildings, The Parade, Cardiff CF24 3AA, UK*
[19]*Department of Physics and Astronomy, University of Turku, FI-20014 Turku, Finland*
[20]*School of Physics, Trinity College Dublin, College Green, Dublin 2, Ireland*
[21]*Istituto di Astrofisica e Planetologia Spaziali (INAF), via del Fosso del Cavaliere 100, I-00133 Roma, Italy*
[22]*The Oskar Klein Centre, Department of Astronomy, AlbaNova, SE-106 91 Stockholm, Sweden*
[23]*Astrophysics Research Centre, School of Mathematics and Physics, Queen's University Belfast, Belfast BT7 1NN, UK*

This paper has been typeset from a TEX/LATEX file prepared by the author.